Ceria–terbia solid solution nanobelts with high catalytic activities for CO oxidation

Gao-Ren Li, Dun-Lin Qu, Zi-Long Wang, Cheng-Yong Su, Ye-Xiang Tong, Laurent Arurault

DOI: 10.1039/b916940g

Ceria–terbia solid solution nanobelts with high catalytic activities for CO oxidation†

Gao-Ren Li,*[a] Dun-Lin Qu,[a] Zi-Long Wang,[a] Cheng-Yong Su,[a] Ye-Xiang Tong*[a] and Laurent Arurault[b]

Ceria–terbia solid solution nanobelts were prepared by an electrochemical route and tested as catalysts of high activity for CO oxidation.

Air pollution has become one of the major global problems. Three-way catalysts (TWC) for automotive exhaust treatment, which can transform three environmentally hazardous gases, namely, CO, NO*x*, and hydrocarbons to environmentally benign or less hazardous form, is therefore a topic of intensive research.[1–5] Ceria-based materials are very important components of promoters for automotive TWCs.[6–9] It is well known that rare earth ion-doped ceria can increase the ionic conductivities,[10] and therefore may generally enhance the catalytic activity of ceria by making oxygen from the bulk more accessible for surface reactions.[11]

As is well known, Ce^{4+} and Ce^{3+} always coexist in CeO_2.[12] The ionic radius of Ce^{3+} ion (1.14 Å) is larger than that of Ce^{4+} ion (0.97 Å) and so the surrounding fluorite lattice will be distorted when Ce^{3+} vacancies are formed in CeO_2. When different +4 cations are doped into the CeO_2 lattice, the oxygen diffusivity within the lattices will be influenced. The energetic cost of these distortions in CeO_2 can be decreased by formation of solid solutions with 4+ ions of smaller size than Ce^{4+} ions, such as Zr^{4+}, Hf^{4+}, Pr^{4+}, Tb^{4+}.[11–15] In addition, the ion mobility inside the CeO_2 lattice will be changed, resulting in the formation of a defective fluorite-structured solid solution. Such modifications in the defect structure of CeO_2 will confer new properties to the catalyst such as high catalytic activity.[16] The use of variable valence dopants in CeO_2 has attracted much attention.[17–18] Herein, special emphasis is given on the influence of Tb^{4+} doping on the catalytic performance of ceria-based mixed oxides. The element Tb can exhibit variable valence states (3+ and 4+), which may have some special impact on the final product.

Constructing novel nanostructures to obtain enhanced properties appears a viable route in designing and selecting catalysts and catalyst promoters for specific catalytic reactions.[19,20] CeO_2-based composites with nanostructures usually have high surface areas, improved sintering properties and high oxygen storage capacities, which may highly enhance the catalytic performance. To the best of our knowledge, there have been no reports on the successful synthesis of one-dimensional ceria-based mixed oxide nanobelts. Herein, detached $Ce_{1-x}Tb_xO_{2-\delta}$ nanobelts are first synthesized by electrochemical deposition at room temperature and usual atmospheric pressure without any surface-capping agent. The $Ce_{1-x}Tb_xO_{2-\delta}$ nanobelts as a new family of CeO_2-based oxide nanostructures are desirable because of their unique physical and chemical properties.[11] The electrochemical deposition is a simple and low-cost route to this material.

In this experiment a simple three-electrode cell was used. A highly pure Pt foil (99.99 wt%, 0.25 cm^2) was used as the auxiliary electrode. A saturated calomel electrode (SCE) was used as the reference electrode that was connected to the cell with a double salt bridge system. The electrochemical deposition was carried out in a solution of 0.01 M $Ce(NO_3)_3$ + 0.001 M $Tb(NO_3)_3$ + 0.1 M NH_4NO_3 with a current density of 4.0 mA cm^{-2} in a configured glass cell at room temperature, in which a Cu plate (99.99 wt%, 0.25 cm^2) served as the substrate. The oxygen was dissolved in the deposition solution through bubbling in the electrolyte. Before electrodeposition, the Cu substrate was cleaned ultrasonically in 0.1 M HCl, distilled water, and acetone and then rinsed in distilled water again. The products were characterized by X-ray diffractometry (D/MAX 2200 VPC with Cu-Kα radiation), and an Oxford Instruments INCA energy-dispersive spectrometer (EDS) was employed to analyze chemical composition. Microstructures of the deposits were characterized by field emission scanning electron microscopy (FE-SEM; JSM-6330-F) and X-ray photoelectron spectroscopy (XPS, ESCALAB 250) was used to assess the chemical state and surface composition of the deposits.

SEM images of $Ce_{1-x}Tb_xO_{2-\delta}$ composites with different magnifications are shown in Fig. 1(a) and (b), which reveal that the deposit consists of a large quantity of nanobelts with length of about 0.5–2.0 μm, width of 100–250 nm and thickness of only about 30 nm. The microstructural details of $Ce_{1-x}Tb_xO_{2-\delta}$ nanobelts were further investigated by TEM as shown in Fig. 1(c) and (d). High-resolution TEM (HRTEM) images of individual nanobelts clearly display lattice fringes for nanocrystals, indicating that these $Ce_{1-x}Tb_xO_{2-\delta}$ nanobelts possess high crystallinity. The measured interplanar spacings from HRTEM are about 0.31 and 0.28 nm, which are in good agreement with (111) and (200) facet distances of the CeO_2 phase, respectively. The SAED pattern (inset in Fig. 1(d)) indicates that the prepared nanobelts have a polycrystalline structure.

[a] *MOE Laboratory of Bioinorganic and Synthetic Chemistry/School of Chemistry and Chemical Engineering/Institute of Optoelectronic and Functional Composite Materials, Sun Yat-Sen University, Guangzhou 510275, P. R. China.*
E-mail: ligaoren@mail.sysu.edu.cn, chedhx@mail.sysu.edu.cn; Fax: 86-20-84112245; Tel: 86-20-84110071
[b] *CIRIMAT-LCMIE, Université Paul Sabatier, 31062 Cedex 9, France*

† Electronic supplementary information (ESI) available: Catalytic activity measurements; characterization; EDS pattern; XPS spectrum; SEM images; TG curves. See DOI: 10.1039/b916940g

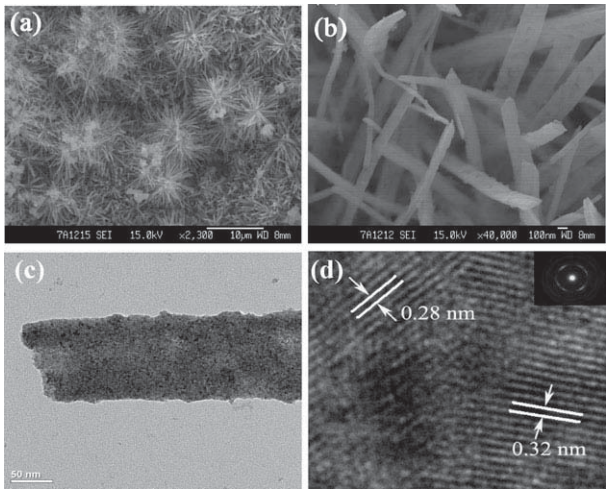

Fig. 1 SEM images of (a) low magnification and (b) high magnification; (c) TEM image; (d) HRTEM image; and SAED (inset) of $Ce_{1-x}Tb_xO_{2-\delta}$ nanobelts prepared in solution of 0.01M $Ce(NO_3)_3$ + 0.001 M $Tb(NO_3)_3$ + 0.1M NH_4NO_3 with current density of 4.0 mA cm^{-2}.

A representative EDS pattern of $Ce_{1-x}Tb_xO_{2-\delta}$ nanobelts is shown in Fig. S1 (ESI†) which revealed O, Ce and Tb to be present. The content of Tb in $Ce_{1-x}Tb_xO_{2-\delta}$ composites was determined to be about 6.5 at.%, and the Ce content is about 93.5 at.%. XPS analyses of $Ce_{1-x}Tb_xO_{2-\delta}$ nanobelts were carried out and the O 1s core level XPS profile is shown in Fig. S2 (ESI†). The peak centered at 530.1 eV corresponds to the O^{2-} contribution, and can be attributed to the lattice oxygen associated with $Ce_{1-x}Tb_xO_{2-\delta}$. Another peak at a slightly lower binding energy side can be attributed to absorbed oxygen species (presumably from absorbed water). It is well known that a small amount of Ce^{3+} coexists at the surface of CeO_2.[21] Two sets of spin–orbit multiplets corresponding to $3d_{3/2}$ and $3d_{5/2}$ are present as peaks labelled *u* and *v*, respectively in Fig. 2(a). The peaks centered at 899.0 eV (u_1), 908.3 eV (u_2) and 917.1 eV (u_3) eV can be attributed to the Ce^{4+} contribution while the peaks centered at 884.2 eV (v_1) and 902.2 eV (v_2) can be attributed to the Ce^{3+} contribution. Thus, the surface of the present samples contains Ce both in the 4+ and the 3+ states. Fig. 2(b) shows the Tb 4d spectrum of a $Ce_{1-x}Tb_xO_{2-\delta}$ nanobelt sample. As the kinetic energies of the photoemitted electrons are very low, Tb 3d core level analysis is very difficult by a conventional laboratory spectrometer (with either Mg or Al KR radiation). Thus the most intense core level (Tb 4d) is used for analysis. There is an agreement that Tb^{3+} gives a signal below 150 eV and Tb^{4+} is related to features well above 150 eV.[22–24] The spectrum in Fig. 2(b) obviously shows a pronounced shoulder below 150 eV, a maximum at 152.3 eV and a tailing toward 160 eV, indicating the presence of more than one oxidation state, *i.e.*, the 3+ and the 4+ oxidation states. Therefore, the XPS results further demonstrated $Ce_{1-x}Tb_xO_{2-\delta}$ composites were successfully synthesized.

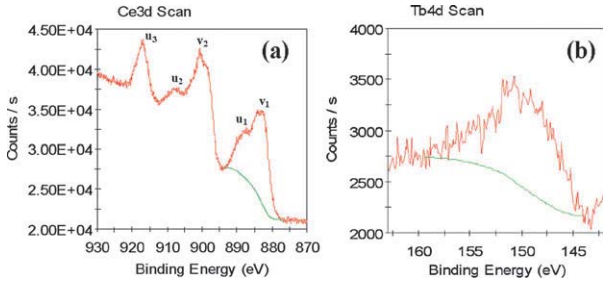

Fig. 2 (a) Ce 3d and (b) Tb 4d core level spectra of $Ce_{1-x}Tb_xO_{2-\delta}$ nanobelts.

Fig. 3(a) shows the XRD pattern of as-prepared $Ce_{1-x}Tb_xO_{2-\delta}$ (x = 6.5 at.%) nanobelts. Peaks corresponding to CeO_2 (111), (200), (220) and (311) planes were observed, indicating a face-centered cubic-phase CeO_2 (JCPDS 34-0394). The diffraction peaks of TbO_2 or Tb_2O_3 were not observed, indicating Tb has entered into the CeO_2 lattice. The calculated cell parameter (a) is equal to 0.5378 nm, a little smaller than that of bulk CeO_2 (0.5411 nm). This may be due to a lattice constriction effect resulting from Tb^{4+} ions as Tb^{4+} has a smaller ionic radius than that of Ce^{4+} (the ionic radii values for Ce^{4+}, Tb^{4+}, Ce^{3+} and Tb^{3+} are 0.97, 0.88, 1.14 and 1.04 Å, respectively).[25] The lattice constriction is additional evidence for the formation of solid solutions. The broadening of the reflections of $Ce_{1-x}Tb_xO_{2-\delta}$ nanobelts in Fig. 3(a) can be attributed to the smaller nanocrystallites. The average crystallite sizes of $Ce_{1-x}Tb_xO_{2-\delta}$ nanobelts were calculated from X-ray line broadening of the (111) reflection using Scherrer's equation ($D = K\lambda/(\beta\cos\theta)$, where λ is the wavelength of the X-ray radiation, K is a constant, θ is the diffraction angle, and β is the full width at half-maximum). The average crystallite size of $Ce_{1-x}Tb_xO_{2-\delta}$ nanobelts was determined to be about 5.5 nm. The peak shift of $Ce_xTb_{1-x}O_{2-\delta}$ (x = 6.5 at.%) nanobelts compared with pure CeO_2 can be estimated as about 0.4°. The XRD pattern of $Ce_{1-x}Tb_xO_{2-\delta}$ nanobelts calcined at 1100 K are shown in Fig. 3(b). The same monophasic composition is retained, and no phase segregation is observed.

The catalytic activity of the $Ce_{1-x}Tb_xO_{2-\delta}$ (x = 6.5 at.%) nanobelts was investigated by performing the CO conversion reaction. Fig. 4 shows the catalytic activities of $Ce_{1-x}Tb_xO_{2-\delta}$ nanobelts, nanoparticles and nanosheets (all x = 6.5 at.%) as a function of reaction temperature (the surface areas of $Ce_xTb_{1-x}O_{2-\delta}$ nanobelts, nanosheets and nanoparticles are about 115, 72 and 23 m^2 g^{-1}, respectively). It can be clearly observed the CO conversion increases with increasing reaction temperature for all samples. For $Ce_{1-x}Tb_xO_{2-\delta}$ nanobelts as catalyst, a 96% CO conversion is achieved at about 913 K. However, only 43 and 57% CO conversions are obtained at

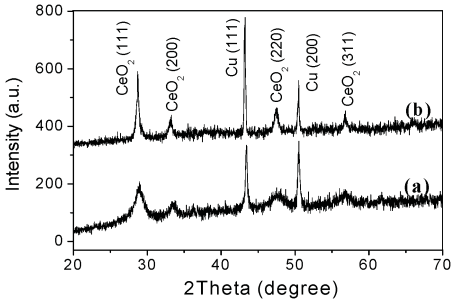

Fig. 3 XRD patterns of the obtained samples: (a) as-prepared $Ce_{1-x}Tb_xO_{2-\delta}$ nanobelts; (b) $Ce_{1-x}T_{-x}O_{2-\delta}$ nanobelts calcined at 1100 K.

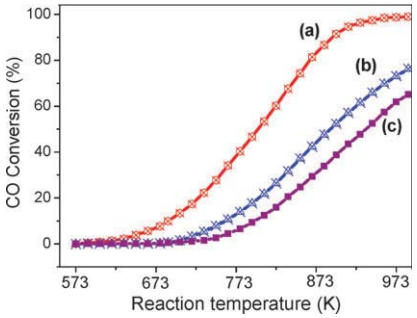

Fig. 4 Conversion of CO over (a) $Ce_{1-x}Tb_xO_{2-\delta}$ nanobelts, (b) $Ce_{1-x}Tb_xO_{2-\delta}$ nanosheets and (c) $Ce_{1-x}Tb_xO_{2-\delta}$ nanoparticles as a function of reaction temperature.

the same temperature for $Ce_{1-x}Tb_xO_{2-\delta}$ nanoparticles and nanosheets as catalysts, respectively. (SEM images of $Ce_{1-x}Tb_xO_{2-\delta}$ nanoparticles and nanosheets are shown in Fig. S3 and Fig. S4, ESI, †respectively) Therefore, the catalytic activity of $Ce_{1-x}Tb_xO_{2-\delta}$ nanobelts is much higher than those of $Ce_{1-x}Tb_xO_{2-\delta}$ nanoparticles and nanosheets. Interestingly, a significant lowering of the starting reduction temperature is noticed for $Ce_{1-x}Tb_xO_{2-\delta}$ nanobelts compared to $Ce_{1-x}Tb_xO_{2-\delta}$ nanoparticles and nanosheets.

Since the components of $Ce_{1-x}Tb_xO_{2-\delta}$ deposits were kept the same, the above different catalytic activities must originate from the different structures that have different oxygen storage capacities (OSCs). As is well known, the value of OSC is a crucial parameter for catalytic activity. Herein, the OSC properties of $Ce_{1-x}Tb_xO_{2-\delta}$ nanobelts, nanoparticles and nanosheets were tested by oxygen release characteristics of the samples calcined at different temperatures under dry air atmosphere in the temperature range 450–1100 K. The change of weight of the sample was monitored by thermogravimetry (TG) under cyclic heat treatments in flowing air. $Ce_{1-x}Tb_xO_{2-\delta}$ samples were subjected to consecutive cycles of heating and cooling, and typical TG curves of various samples were shown in Fig. S5 (ESI†). In the above results, a large decrease of weight was observed in the first heat treatment (A → B) and this can be attributed to the release of both water molecules and oxygen from $Ce_{1-x}Tb_xO_{2-\delta}$ solid solutions. In the cooling back stage (B → C), a partial recovery of the weight of $Ce_{1-x}Tb_xO_{2-\delta}$ sample was observed. In the second heating cycle (C → B), a small decrease of weight was also observed corresponding to the potential oxygen release capacity of the powders in ordinary air atmosphere.[12] The $Ce_{1-x}Tb_xO_{2-\delta}$ nanobelts show the highest weight loss, which is followed by $Ce_{1-x}Tb_xO_{2-\delta}$ nanosheets and nanoparticles. Accordingly the $Ce_{1-x}Tb_xO_{2-\delta}$ nanobelts have the highest OSC among various $Ce_{1-x}Tb_xO_{2-\delta}$ nanostructures. These results are consistent with the catalytic activity order of CO oxidation, where $Ce_{1-x}Tb_x\ O_{2-\delta}$ nanobelts showed better activity than that of $Ce_{1-x}Tb_xO_{2-\delta}$ nanosheets, followed by $Ce_{1-x}Tb_xO_{2-\delta}$ nanoparticles.

In summary, a novel design of ceria–terbia solid solution nanobelts led to catalysts of high activity for CO oxidation. $Ce_{1-x}Tb_xO_{2-\delta}$ nanobelts (x = 6.5 at.%) have been synthesized by electrochemical deposition at room temperature and ordinary atmospheric pressure without any surface capping agent. The electrochemical deposition route shows a facile and low-cost route. The results of XRD and TEM show $Ce_{1-x}Tb_xO_{2-\delta}$ nanobelts are well crystallized and have a cubic structure. A strong shape/crystal structure effect of $Ce_{1-x}Tb_xO_{2-\delta}$ composites for the catalytic activity has been identified. The $Ce_{1-x}Tb_xO_{2-\delta}$ nanobelts are most active for the CO conversion reaction compared with $Ce_{1-x}Tb_xO_{2-\delta}$ nanoparticles and nanosheets. The high catalytic activity of $Ce_{1-x}Tb_xO_{2-\delta}$ nanobelts can be attributed to the special nanostructures with high OSC. These findings can be extended to new studies of other ceria-based mixed oxides with high surface areas.

This work was supported by NSFC (20603048, 20873184 and 90923008) and Guangdong Province (2008B010600040 and 9251027501000002).

Notes and references

1 J. Kašpar, P. Fornasiero and M. Graziani, *Catal. Today*, 1999, **50**, 285–298.
2 H. S. Gandhi, G. W. Graham and R. W. McCabe, *J. Catal.*, 2003, **216**, 433–442.
3 J. Kašpar, P. Fornasiero and N. Hickey, *Catal. Today*, 2003, **77**, 419–449.
4 M. Yang, M. Shen, J. Wang, J. Wen, M. Zhao, J. Wang and W. Wang, *J. Phys. Chem. C*, 2009, **113**, 12778–12789.
5 W. Wang, P. Lin, Y. Fu and G. Cao, *Catal. Lett.*, 2002, **82**, 19–27.
6 G. Kim, *Ind. Eng. Chem. Prod. Res. Dev.*, 1982, **21**, 267–274.
7 N. Hickey, P. Fornasiero, R. Di Monte, J. Kašpar, J. R. González-Velasco, M. A. Gutiérrez-Ortiz, M. P. González-Marcos, J. M. Gatica and S. Bernal, *Chem. Commun.*, 2004, 196–197.
8 B. M. Reddy, P. Bharali, P. Saikia, A. Khan, S. Loridant, M. Muhler and W. Grünert, *J. Phys. Chem. C*, 2007, **111**, 1878–1881.
9 M. Shen, M. Yang, J. Wang, J. Wen, M. Zhao and W. Wang, *J. Phys. Chem. C*, 2009, **113**, 3212–3221.
10 (*a*) H. Yahiro, K. Eguchi and H. Arai, *Solid State Ionics*, 1989, **36**, 71; (*b*) K. Eguchi, T. Setoguchi, T. Inoue and H. Arai, *Solid State Ionics*, 1992, **52**, 165.
11 G. Zhou and R. J. Gorte, *J. Phys. Chem. B*, 2008, **112**, 9869–9875.
12 Be. M. Reddy, P. Lakshmanan, P. Bharali, P. Saikia, G. Thrimurthulu, M. Muhler and W. Gru1nert, *J. Phys. Chem. C*, 2007, **111**, 10478–10483.
13 Q. Yuan, Q. Liu, W.-G. Song, W. Feng, W.-L. Pu, L.-D. Sun, Y.-W. Zhang and C.-H. Yan, *J. Am. Chem. Soc.*, 2007, **129**, 6698.
14 (*a*) W. Chun, G. W. Graham, J. A. Lupescu, R. W. McCabe, M. M. Koranne and R. Brezny, *Catal. Lett.*, 2006, **106**, 95; (*b*) M. Y. Sinev, G. W. Graham, L. P. Haack and M. Shelef, *J. Mater. Res.*, 1996, **11**, 1960.
15 B. M. Reddy, P. Bharali, P. Saikia, S.-E. Park, M. W. E. van den Berg, M. Muhler and W. Grünert, *J. Phys. Chem. C*, 2008, **112**, 11729.
16 (*a*) S. Bernal, G. Blanco, M. A. Cauqui, M. P. Corchado, C. Larese, J. M. Pintado and J. M. Rodŕiguez-Izquierdo, *Catal. Today*, 1999, **53**, 607–612; (*b*) S. Bernal, G. Blanco, M. A. Cauqui, P. Corchado, J. M. Pint-ado and J. M. Rodríguez-Izquierdo, *Chem. Commun.*, 1997, 1545–1546.
17 G. Blanco, J. J. Calvino, M. A. Cauqui, P. Corchado, C. López-Cartes, C. Colliex, J. A. Pérez-Omil and O. Stephan, *Chem. Mater.*, 1999, **11**, 3610–3619.
18 (*a*) X. Wang, J. C. Hanson, G. Liu, J. A. Rodriguez, A. Iglesias-Juez and M. Fernández-García, *J. Chem. Phys.*, 2004, **121**, 5434; (*b*) X. Wang and R. J. Gorte, *Appl. Catal., A*, 2003, **247**, 157–162.
19 F. Zhang, S.-W. Chan, J. E. Spanier, E. Apak, Q. Jin, R. D. Robinson and I. P. Herman, *Appl. Phys. Lett.*, 2002, **80**, 127.
20 J. Rodriguez, J. C. Hanson, J.-Y. Kim and G. Liu, *J. Phys. Chem. B*, 2003, **107**, 3535.
21 Z. Wang, Z. Quan and J. Lin, *Inorg. Chem.*, 2007, **46**, 5237.
22 H. X. Dai, C. F. Ng and C. T. Au, *J. Catal.*, 2001, **199**, 177.
23 G. Blanco, J. M. Pintado, S. Bernal, M. A. Cauqui, M. P. Corchado, A. Galtayries, J. Ghijsen, R. Sporken, T. Eickhoff and W. Drube, *Surf. Interface Anal.*, 2002, **34**, 120.
24 L. Li, Q. Wei, H. Li, D. Zhang and W. Z. Su, *Phys. B*, 1995, **96**, 451.
25 A. B. Hungria, A. M. Arias, M. F. Garcia, A. I. Juez, A. G. Ruiz, J. J. Calvino, J. C. Conesa and J. Soria, *Chem. Mater.*, 2003, **15**, 4309.